Genes & Diseases

FULL LENGTH ARTICLE

Development of a multicellular 3D-bioprinted microtissue model of human periodontal ligament-alveolar bone biointerface: Towards a pre-clinical model of periodontal diseases and personalized periodontal tissue engineering

Murat Taner Vurat [a],[1], Şükran Şeker [a],[1], Özge Lalegül-Ülker [a], Mahmut Parmaksiz [a], Ayşe Eser Elçin [a], Yaşar Murat Elçin [a],[b],[*]

[a] *Tissue Engineering, Biomaterials and Nanobiotechnology Laboratory, Ankara University Faculty of Science, Ankara University Stem Cell Institute, Ankara 06100, Turkey*
[b] *Biovalda Health Technologies, Inc., Ankara 06100, Turkey*

Abstract While periodontal (PD) disease is among principal causes of tooth loss worldwide, regulation of concomitant soft and mineralized PD tissues, and PD pathogenesis have not been completely clarified yet. Besides, relevant pre-clinical models and *in vitro* platforms have limitations in simulating human physiology. Here, we have harnessed three-dimensional bioprinting (3DBP) technology for developing a multi-cellular microtissue model resembling PD ligament-alveolar bone (PDL-AB) biointerface for the first time. 3DBP parameters were optimized; the physical, chemical, rheological, mechanical, and thermal properties of the constructs were assessed. Constructs containing gelatin methacryloyl (Gel-MA) and hydroxyapatite-magnetic iron oxide nanoparticles showed higher level of compressive strength when compared with that of Gel-MA constructs. Bioprinted self-supporting microtissue was cultured under flow in a microfluidic platform for >10 days without significant loss of shape fidelity. Confocal microscopy analysis indicated that encapsulated cells were homogenously distributed inside the matrix and preserved their viability for >7 days under microfluidic conditions. Immunofluorescence analysis showed the cohesion of stromal cell surface marker-1+

---

* Corresponding author. Ankara University, Faculty of Science, Biochemistry Division, Tandogan, Ankara 06100, Turkey. Fax: +90 312 223 2395.
E-mail addresses: elcinmurat@gmail.com, elcin@ankara.edu.tr (Y.M. Elçin).
Peer review under responsibility of Chongqing Medical University.
[1] These authors contributed equally to this article.

human PDL fibroblasts containing PDL layer with the osteocalcin+ human osteoblasts containing mineralized layer in time, demonstrating some permeability of the printed constructs to cell migration. Preliminary tetracycline interaction study indicated the uptake of model drug by the cells inside the 3D-microtissue. Also, the non-toxic levels of tetracycline were determined for the encapsulated cells. Thus, the effects of tetracyclines on PDL-AB have clinical significance for treating PD diseases. This 3D-bioprinted multi-cellular periodontal/osteoblastic microtissue model has potential as an *in vitro* platform for studying processes of the human PDL.

Introduction

The periodontal ligament (PDL) is a unique specialised fibrous network connecting the mineralized surfaces, i.e., alveolar bone (AB) and tooth root. PDL, AB and the cementum are intimately related structures which form the periodontium. These structures play an important role in orthodontic tooth movement, homeostatic maintenance of tooth supporting apparatus and can be adversely affected by periodontal diseases.[1] PDL consists of numerous cell types, including PDL fibroblasts (PDLFs), osteoblasts (OBs), cementoblasts, progenitor cells, etc. With its array of oriented fibres, PDL supports the periodontium as a shock absorber. It also functions as a barrier for pathogens and provides sensory input for the mastication system. PDL also functions as a renovator for the destructed tissue caused by periodontal disease or mechanical trauma, acting as a pool of adult stem cells for regenerating periodontal tissues.[2]

Periodontal (gum) disease involving inflammatory response is one of the principal causes of tooth loss worldwide.[3] Periodontitis, the advanced stage of periodontal disease has major effects on public health, with almost 10% of the global population affected.[4] This prevalent condition affects both the soft and mineralized periodontal tissues concomitantly and results with the formation of periodontal pockets harbouring periodontal pathogenic microorganisms that perpetuate the inflammatory destructive disease. A great number of studies have evaluated the cell types, cellular interactions, and major biological processes between the PDL and AB.[5] For example, the osteogenic differentiation of human PDLFs (hPDLFs) have been evaluated in two- (2D) and three-dimensional (3D) culture systems.[6] hPDLFs encapsulated in chitosan-hydroxyapatite (HAp) microspheres were tested as a mineralized 3D culture platform.[7] hPDLF progenitors seeded on nanofibrous polymeric substrates have been proposed as a model culture system.[8] 3D-PDLF spheroids have been used to investigate the osteogenic and cementogenic potential of these progenitors.[9] However, development and regulation of the PDL lineage, the periodontal pathogenesis and AB remodeling have not been completely clarified yet.

Some advances have been made in pre-clinical models for studying periodontal pathogenesis.[10,11] However, there is a consensus that animal models, while informative, are inadequate to accurately simulate human physiology, both in health and disease.[12,13] This is an essential issue in most drug development processes encountering high failure rate in clinical trials.[14] Besides, *in vitro* modeling of human physiology is another challenging objective with conventional 2D or 3D cell culture platforms. Thus, there is a necessity to develop biomimetic and reliable platforms which can complement the current approaches based on cell cultures and experimental animal models.[15]

Multi-cellular 3D tissue models have emerged with the aim to emulate cellular systems or processes in micro scale, usually involving microfluidic and microfabrication techniques.[16,17] They have the potential to overcome significant shortcomings of the current *in vitro* and *in vivo* testing platforms by aid of tissue engineering.[18] Already, a number of tissues and organs have been developed as multi-cellular models for healthy or disease conditions with unprecedented success, for example the heart, skin and intestine.[19–21] In addition, platforms simulating functional biological systems and conditions, such as the female reproductive system, blood–brain-barrier, and a variety of cancers have also been successfully developed.[22–24] However, a 3D multi-cellular tissue model emulating the periodontal ligament-alveolar bone biointerface (Fig. S1) has not been developed to date.

3D-Bioprinting (3DBP) permits the fabrication of biomimetic tissue microarchitectures by using viable cells and biological molecules by aid of an ECM-analogue bioink in gel form.[25–29] Initially, the driving force of this technology has been to develop tissues or organs for transplantation, later on it has also been utilized for building 3D complex microtissues with high spatial and temporal resolution.[30–32] Raveendran et al[33] have evaluated gelatin methacryloyl (Gel-MA) as a bioink for the bioprinting of PDL cells, however they have not attempted to juxtapose PDL and AB structures.

Tetracyclines are a class of the antibiotics that are used as adjuncts to periodontal debridement and surgical treatments due to their antimicrobial spectrum and high affinity binding to the mineralized tissues such as bone.[34] It has also been demonstrated that subantimicrobial low dose of doxycycline inhibits the inflammatory response and prevents the exacerbation of the inflammation-mediated periodontal tissue destruction.[35] Thus, the effects of the tetracyclines on periodontal ligament and alveolar bone-derived cells has a prominent clinical significance for the treatment of periodontal diseases.

This study combines the use of 3D-bioprinting technology for developing a human 3D periodontal/osteoblastic microfluidic tissue model for the first time. Periodontal ligament layer has been modelled by using Gel-MA bioink for bioprinting the hPDLFs. On the other hand, the alveolar bone layer has been modelled by using a composite bioink comprised of Gel-MA and HAp-magnetic iron oxide nanoparticles (Gel-MA/HAp-MNPs) for bioprinting the human OBs. HAp has been included to Gel-MA to simulate the bone inorganic composition, whereas MNPs have been incorporated for obtaining magnetic properties for use in prospective mechanotransductive studies simulating orthodontic movement. The 3DBP parameters were optimized; then the physical, chemical, rheological, mechanical, and thermal properties of the microtissue constructs were assessed. Finally, preliminary evaluation of the uptake and toxicity of the model drug tetracycline on human periodontal/osteoblastic tissue model was performed using a microfluidic circulation system.

Materials and methods

Synthesis of MNPs and HAp-MNPs

Magnetic nanoparticles (MNPs) were synthesized by following the co-precipitation method.[36] For this purpose, aqueous solutions of 2 mmol $FeCl_3.6H_2O$ and 1 mmol $FeCl_2.4H_2O$ were mechanically mixed under nitrogen atmosphere. A 25% solution of NH_4OH was added dropwise to the solution until pH reached a value of 11. The obtained MNPs were then magnetically separated from the solution and washed several times with deionized water and ethanol, respectively. MNPs were dried overnight at 40 °C and subsequently stored at room temperature.[37]

To obtain the composite nanostructures, the MNPs were suspended in 1 M $Ca(NO_3)_2$ solution and added dropwise into a solution of 0.6 M $(NH_4)_2HPO_4$. pH was adjusted to 11 by adding 25% solution of NH_4OH. The mixture was stirred at room temperature for 5 h, and then kept still for about 24 h at room temperature.[38] HAp-coated MNPs were separated from non-magnetic HAp by magnetic decantation and then dried at 40 °C for 24 h. All chemicals were purchased from Sigma—Aldrich (St. Louis, MO, USA), unless otherwise stated.

Synthesis of Gel-MA and preparation of the bioinks

Methacrylated gelatin (Gel-MA) was synthesized by reaction of gelatin (type A, from porcine skin; gel strength 300, Sigma) with methacrylic anhydride (94% from Sigma) as previously described.[39] Briefly, 5 g of gelatin was dissolved in 50 mL Dulbecco's phosphate-buffered saline (DPBS; pH 7.4) at 50 °C until completely dissolved. 8 mL of methacrylic anhydride was added to the gelatin solution under constant stirring at a rate of 0.5 mL/min and allowed to react for 3 h. Later, the mixture was diluted (1:5) by adding warm DPBS at 40 °C to stop the reaction. The solution was then dialyzed against distilled water using a dialysis tubing (12—14 kDa cut-off) at 40 °C for 5 days to remove unreacted residues. The product was freeze-dried for 1 week and stored at −80 °C until further use.

Gel-MA bioink (12.5 wt-%) was prepared by dissolving the lyophilized Gel-MA macromer in PBS (pH:7.4) containing 0.5 wt-% of radical photoinitiator (2-hydroxy-4′-(2-hydroxyethoxy)-2-methylpropiophenone; Irgacure 2959, Sigma) at 60 °C and passing through sterile syringe filter (0.2 μm pore size). The composite Gel-MA/HAp-MNP bioink was obtained by incorporating 0.1% of UV-sterilized HAp-MNPs in the 12.5% Gel-MA solution, and mixing until a completely homogeneous blend was formed. Increasing amounts of HAp-MNPs caused clogging of the nozzle during the bioprinting process as a result of agglomeration of nanoparticles. Therefore, the concentration of HAp-MNPs was set to 0.1%, which was found suitable. The air bubbles were removed by sonication before loading the sterile bioinks into the syringes for bioprinting.

Characterization of MNPs and HAp-MNPs

TEM
The size, coating efficiency, nanoparticle distribution and morphological features of both MNPs and HAp-MNPs were evaluated by using a FEI Tecnai G2 Spirit Biotwin model transmission electron microscope (TEM; Hillsboro, OR, USA). Nanoparticle powders were sonicated in ethanol and 5—10 μL of the suspension was dropped onto carbon-coated copper grids. All samples were air-dried before analysis.

FTIR
ATR-FTIR spectroscopy analysis was performed to identify the functional groups related to iron oxide and HAp, in the spectral range of 600—4000 cm^{-1} by using a Shimadzu IRAffinity system (Kyoto, Japan).

VSM
The magnetic properties of MNPs and HAp-MNPs were measured using the vibrating sample magnetometry (VSM), after drying the MNPs and HAp-MNP powders at 40 °C and analyzing at room temperature using a Cryogenic Limited PPMS device (London, UK).

Optimization of 3D-bioprinting with the bioinks

Two layered grid model was designed by using Computer-Aided Design (CAD) software and slicing process was performed using Slic3r software (version 1.2.9). A commercial pneumatic extrusion bioprinter (Inkredible+, Cellink, Gothenburg, Sweden) was used for the 3D-bioprinting of Gel-MA and Gel-MA/HAp-MNP bioinks on the designed 3D model. All printings were performed at room temperature using 27G sterile polypropylene high-precision conical nozzles. During the entire process, the nozzle movement speed was set to 5 mm.s^{-1}, the extrusion pressure was manually controlled and set to ~55 kPa and infill density was set to 100%. The optimal parameters for the 3D-bioprinting process are listed in Table S1.

The designed and produced microfluidic chips were placed at the appropriate coordinates on the bioprinter platform and *in situ* 3DBP was performed on chip reservoirs. The printed Gel-MA and Gel-MA/HAp-MNP composite model constructs were exposed to UV light (365 nm) at a

distance of 10 cm for 120 s for photo-crosslinking right after the 3D-bioprinting process.

Characterization of Gel-MA and Gel-MA/HAp-MNP bioinks

Rheology
The rheological properties of Gel-MA and Gel-MA/HAp-MNP bioinks were evaluated by an Anton Paar Rheoplus32 model rheometer (Graz, Austria), after placing the samples between parallel plates of the device. The measurements of the storage modulus (G′) and the loss modulus (G″) were performed with a temperature scan ranging from 40 °C to 10 °C at a cooling rate of 1 °C/min.

FTIR
ATR-FTIR analysis was performed to investigate the chemical composition of photo-cross-linked cell-free constructs using the IRAffinity system (Shimadzu). The specimens were frozen at −80 °C, and lyophilized. Spectral findings were collected in the range of 4000 cm^{-1} and 600 cm^{-1} wavelength, with a resolution of 16 cm^{-1} at 64 scans.

Thermogravimetric analysis
The thermal stability of the two-layer photo-crosslinked cell-free constructs was investigated by using a DTG-60/60 model thermogravimetric analyzer (Shimadzu). Lyophilized specimens were analyzed in the temperature range from 30 to 600 °C at a heating rate of 25 °C/min under dynamic nitrogen atmosphere.

Mechanical analysis
The mechanical properties of photo-cross-linked cell-free constructs were investigated by a compression test using an AGS-X model universal test machine with 500 N load capacities (Shimadzu). The tests were carried out at a strain of 50% and the drawing speed was set to 1 mm/min. The assay was performed at room temperature and on four replicates for each sample tested. The averages of obtained data were given as the stress—strain curve.

SEM
The surface morphology of the two-layered (Gel-MA on Gel-MA/HAp-MNPs), photo-cross-linked constructs was evaluated by using a Quanta 400F model scanning electron microscope (FEI Instruments, Hillsboro, OR, USA). The samples were lyophilized, then were sputter-coated with gold using an automatic sputter coater for 60 s to form a conductive film layer, and were imaged at different magnifications, at 10 kV accelerating voltage.

Swelling testing
Swelling test was performed to evaluate the buffer retention capacity and dissolution properties of photo-cross-linked cell-free Gel-MA or Gel-MA/HAp-MNP comprising different concentrations (0.1, 0.25, 0.5% w/v) of photoinitiator. These also were the photoinitiator concentrations evaluated during the optimization of 3DP (not given). Measurements were done by the weighing method using disk-shaped samples (h:2 mm, Ø:15 mm). At first, the initial dry weights (W_1) were determined; then the

samples were inserted into tubes containing 15 mL of PBS (pH 7.4) at 37 °C for 48 h to reach equilibrium swelling. The disks were removed at defined time points, excess buffer on the surfaces were gently blotted, and swollen weights (W_2) were determined. Buffer retention capacity (BRC %) was calculated by weight gain caused by fluid retention as given in Eq. (1).

$$BRC\% = [(W_2 - W_1)/W_1] \times 100 \qquad \text{Eq.1}$$

Chips and microfluidic system
Microfluidic chip system was designed as two separate layers with inlet, outlet and reservoir components. The layers were made up of polydimethylsiloxane (PDMS; Sylgard 184 and curing agent, Dow Corning, Midland, MI, USA), and were produced by using the soft lithography method. Two layers were immobilized with a special cover platform and stainless steel screws to avoid leakage. While the reservoir and microchannels were located in the bottom layer of the chip, inlet and outlet holes were located in the top layer. Sterile silicone tubing with an inner diameter of 1 mm was used for medium flow. Connectors suitable for the silicone tubing were produced by 3D-printing to fit perfectly, and were used at the inlet and outlet holes of the chip. All components of the microfluidic system were resistant to steam sterilization for at least 10 cycles, and were autoclaved prior to the microfluidic culture stage. The circular reservoir had a depth of 1.5 mm and a surface area of ~176.6 mm^2 (with a total working volume of ~265 mm^3). The chamber had rounded corners and tapered edges to reduce both stagnation and turbulent zones. This feature is also known to minimize bubble formations.

Culture of hPDLFs and hOBs
Human PDLFs were obtained from Lonza (CC-7049, Clonetics™, Basel, Switzerland). hPDLFs were cultured in DMEM-F12 (Dulbecco's modified Eagle's medium Ham's F12; Lonza) supplemented with 10% fetal bovine serum (FBS), 2 mM L-glutamine (Gibco, ThermoFisher, Waltham, MA, USA), 100 μL/mL penicillin-streptomycin (Lonza) inside a CO_2 incubator adjusted to 37 °C, 5% CO_2 and 95% humidity.[40]

Human osteoblasts (hOBs) were obtained from American Type Culture Collection (hFOB 1.19; ATCC® CRL11372™, Manassas, VA, USA). hOBs were cultured in DMEM-F12 (1:1) supplemented with 10% FBS, 2 mM L-glutamine, 100 μL/mL penicillin-streptomycin in the CO_2 incubator at 37 °C.

The media of both cell cultures were changed every 2—3 days with fresh medium. Cell morphologies were monitored under an inverted microscope (Primo Vert, Zeiss, Germany). After the cells reached ~80% confluence, they were passaged as required to reach the needed cell numbers for the subsequent experiments.

3D-bioprinting with cells
The main stages of 3D-bioprinting cells with the relevant bioinks are shown in Figure 1. A final density of 4.0 × 10^6 cells/mL gel was chosen for bioprinting both of the cell types according to previous studies.[29] hPDLFs were mixed with the Gel-MA bioink for bioprinting the
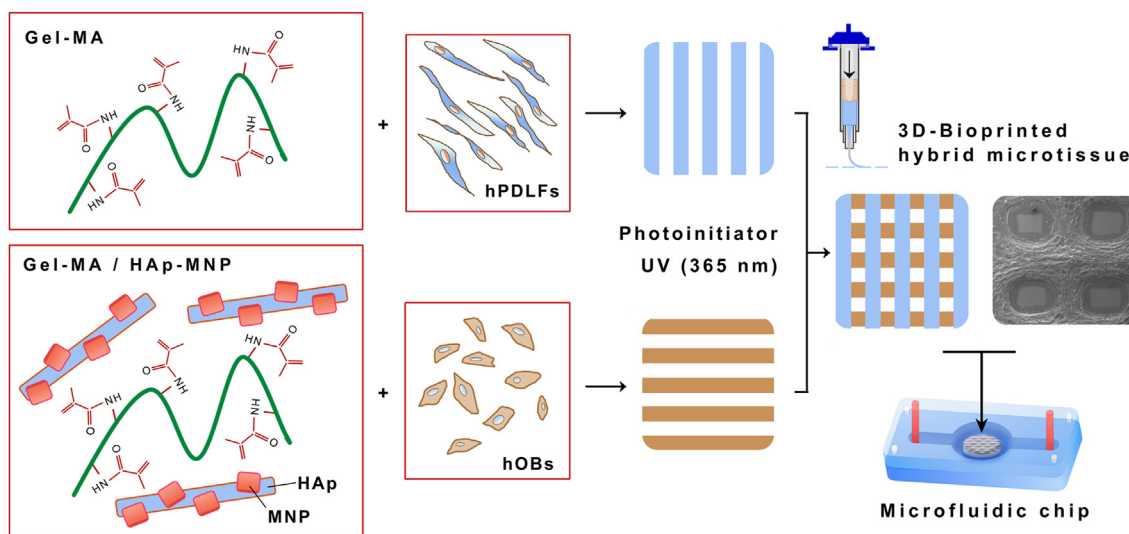
Figure 1 Schematic showing the 3D bioprinting of cells with the relevant bioinks. hPDLFs suspended in Gel-MA were bioprinted as the top periodontal layer, whereas hOBs suspended in Gel-MA/HAp-MNP were bioprinted as the bottom alveolar bone layer. The hybrid hydrogels contained the radical photoinitiator and were stabilized by UV light at a wavelength of 365 nm to form the 3D-bioprinted periodontal/osteoblastic microtissue construct within the microfluidic chip.

periodontal layer (simulating periodontal ligament), on the other hand hOBs were mixed with the Gel-MA/HAp-MNP bioink for bioprinting the osteogenic layer (simulating alveolar bone). Briefly, cells suspended in 200 μL of medium were mixed with the relevant bioink using the cellmixer device (Cellink) and loaded into the filling cartridges simultaneously. Cell-laden bioinks were placed alongside in the pneumatic extrusion bioprinter (Inkredible+, Cellink) located inside a sterile cabinet for implementing the 3D-bioprinting process. 27G (ø: 0.2 mm) polypropylene conical nozzles (Cellink) were used for the 3DP of the bioinks. The cell-laden bioinks were *in situ* bioprinted inside the reservoir of the sterilized chip placed at the appropriate co-ordinates on the bioprinter platform, starting with the osteogenic layer and continuing with the periodontal layer. The composite gels were photo-cross-linked (by exposure to UV light at 365 nm) in between and at the end of the two printings (120 s each at a distance of 10 cm) to generate the microtissue constructs.

Microfluidic culture of the constructs

The scheme of the microfluidic chip and the culture medium circulation system used in the study is presented in Figure 2. The chip housing the 3D-bioprinted microtissue (microbioreactor) was immobilized with the PDMS cover and tightened by a set of screws and bolts to seal the device, and connected through silicone tubings to the integrated circulation system, consisting of a peristaltic pump, silicone tubing with an inner diameter of 1 mm, and separate bottles containing the fresh and used culture media. The flow rate of the medium was set at 300 μL/min, taking into consideration the reservoir volume ($\sim$265 mm^3) and the mechanically dynamic nature of the tissue. This flow rate is towards the upper limit of applied flow rates (usually $\sim$10—500 μL/min) in comparable studies. The circulation system was placed inside an incubator adjusted to 37 °C, 5% CO_2-95% air and 95% humidity. The cultured microtissues

and/or the waste medium were retrieved at set time points for analyses.

Characterization of microtissue constructs

Alamar blue assay

Cell viability was measured by the Alamar blue assay. Hybrid microtissue cultured in the microfluidic system were taken from the reservoir of the chip at predetermined time points (1, 3 and 7 days) and placed in a 24-well plate. After washing with PBS, the samples were incubated with Alamar blue reagent (1/10) in serum-free medium for 4 h at 37 °C in dark. Cell-free hybrid microtissues were used as control. At the end of the incubation period, 200 μL of samples were transferred to a 96-well plate. Fluorescent intensities (Ex: 570 nm, Em: 585 nm) were measured using a SpectraMax® M5 model microplate reader (Molecular Devices, San Jose, CA, USA). The groups were compared with time change using the two-way ANOVA and Bonferroni post-hoc test ($^*P < 0.05$) for $n \geq 3$ individual repeats.

Live/dead cell staining

Live/dead staining was performed on the cultured microtissues inside the microfluidic chip after 12 h, 3 and 7 days of cell seeding. After the washing process, microtissues were incubated with staining solution prepared in PBS containing 4 μM ethidiumhomodimer-1 and 2 μM calcein AM (Live/Dead® Viability/Cytotoxicity kit; Invitrogen) for 45 min in dark at room temperature. At the end of the incubation, the samples were analysed by a LSM 880 inverted laser scanning confocal microscope (Carl Zeiss, Germany) and cell viability and distribution were monitored.

Immunofluorescence analysis

Immunofluorescence (IF) analysis was carried out to determine the distribution and characteristic expressions of
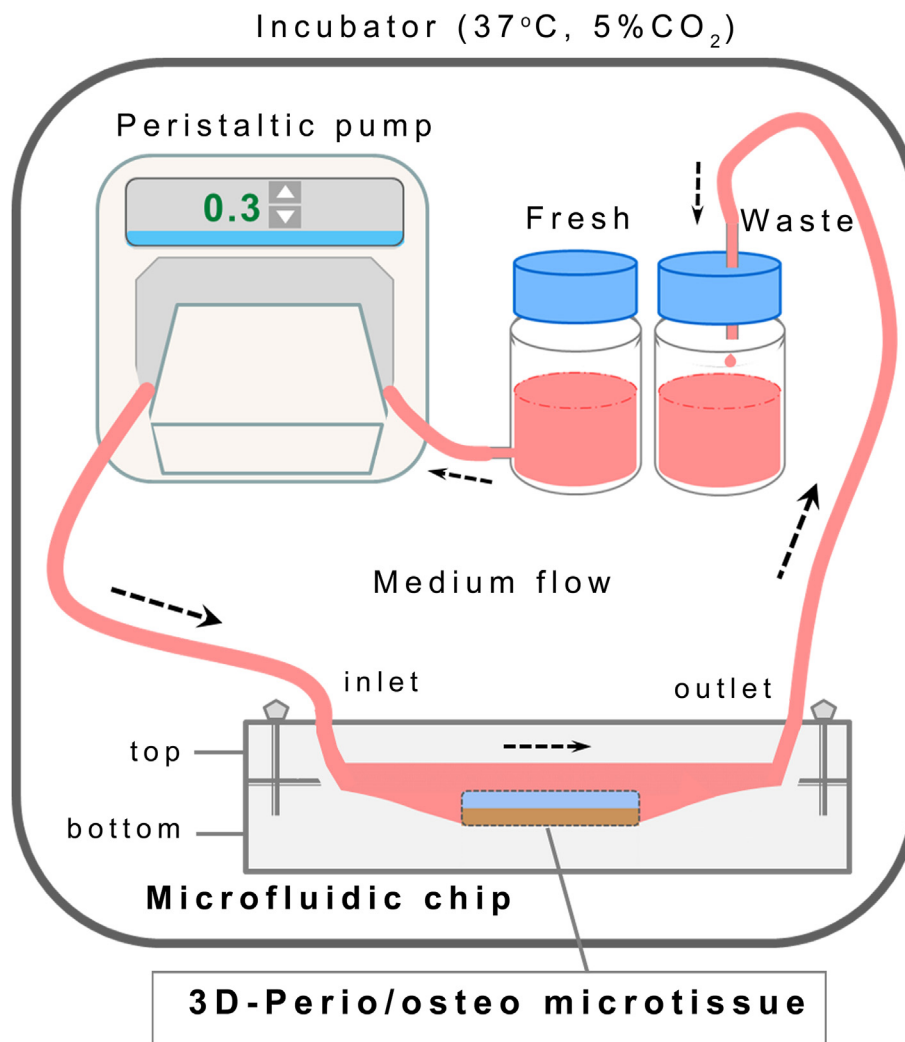
Figure 2 Schematic demonstration of the microfluidic chip and the culture medium circulation system used in the study.

the cells in the perio/osteo microtissue cultured in the microfluidic system. Microtissues were retrieved from the reservoir at determined time points (after 1, 3 and 7 days) and fixed in a 10% formaldehyde solution. Then, the samples were processed for cryosection as described above. The sections were stained with immunofluorescent markers, STRO-1 for hPDLFs and osteocalcin (OC) for hOBs. Sections were washed in PBS for 5 min and immersed in a blocking solution containing 0.1% Triton X-100 and 1% bovine serum albumin. Thereafter, the sections were incubated with primary antibody solution. After washing with PBS, they were incubated with a secondary antibody solution at room temperature. Finally, the stained sections were imaged using an Axio Vert A1 model fluorescence microscope (Carl Zeiss, Germany).

Tetracycline interactions

Human periodontal/osteoblastic microtissue exposed to tetracycline in microfluidic culture was evaluated by using the Alamar blue cell viability assay, histochemical (PAS) staining, tetracycline absorption and CLM (live/dead) analyses. Microtissues were exposed to different doses of

tetracycline for toxicity evaluation, within the commonly used range of $0-1.0$ µg/mL in microfluidic culture.[41] Another reason for selecting this dose range was that the plasma peak concentration of tetracycline is known to be around 1 µg/mL after systemic administration of the usual therapeutic doses.[42]

Histochemical analyses were carried out to evaluate the distribution of cells and the encapsulation matrix in the 3D-bioprinted microtissues cultured inside the microfluidic chip. For that, cell-laden hybrid microtissues were removed from the chip reservoir at determined time points (days 3 and 7), and fixed in 2.5% glutaraldehyde. After the fixation process, the samples were immersed in 15% sucrose solution for 30 min, embedded in optimal cutting temperature compound (Tissue-Tek, Sakura, Zuid-Holland, Netherlands) and stored at -80 °C. Then, $4-5$ µm frozen sections were cut using a Leica cryostat (CM 1900, Nussloch, Germany). The sections were stained with Periodic Acid Schiff (PAS) staining and visualized by a light microscope (Leica, Wetzlar, Germany).

The determination of drug absorption was conducted using the waste medium of the cultured periodontal/

osteoblastic microtissue in the presence of 0.1 μg/mL of tetracycline. Cell-devoid gels served as control. The media were collected at predetermined time intervals and stored −80 °C until use. The drug absorption levels of the hybrid microtissues were determined by using the tetracycline ELISA kit (BioVision) in accordance with the standard kit protocol.

Subcutaneous implantation of acellular constructs

The *in vivo* histocompatibility and degradation properties of the 3D-bioprinted acellular constructs were evaluated subcutaneously at the epigastric groin fascia of adult Wistar rats (weighing 275 ± 50 g; *n* = 4) in accordance with the international guidelines and institutional approval (2016-12-133). The surgical procedures[43] were performed in aseptic conditions under anesthesia by intraperitoneal injection with ketamine hydrochloride (60 mg/kg) and xylazine (10 mg/kg). The sites were shaved, disinfected with iodine and isopropyl alcohol, and incisions were made at the right and left groins. Sterile acellular constructs were then placed in the formed flaps and the incisions were closed by sutures. The subjects were sacrificed after 15 and 30 days post-implantations, then routine histology

was performed on hematoxylin-eosin (H&E)-stained specimens, and the sections were evaluated by a light microscope.

Statistical analysis

All experiments were performed in triplicate, unless otherwise stated. The data were presented as mean ± standard deviation. In statistical analyses, Graph-Pad Prism5 (GraphPad Software, La Jolla, CA, USA) was used for one-way ANOVA and two-way ANOVA tests.

Results and discussion

Characterization of MNPs and HAp-MNPs

TEM micrographs of MNPs and HAp-MNPs are shown in Figure 3A. It is clear from the figure that the MNPs have a spherical shape with an average size of ∼15 nm. Magnetic nanoparticles tend to agglomerate due to the magnetic forces and their size in nanoscale (left image). It is also observed that the needle-shaped HAp nanorods are formed
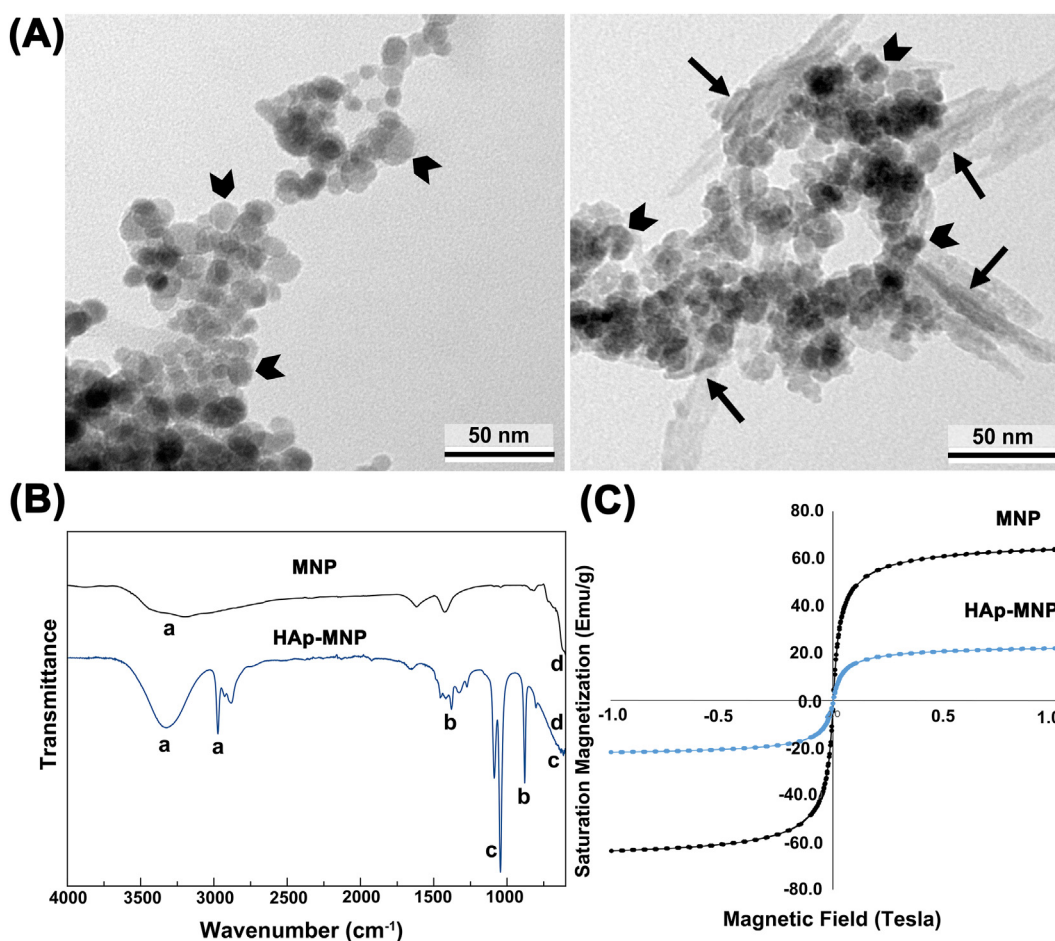
Figure 3 Characterization of MNPs and HAp-MNPs. **(A)** TEM micrographs. MNPs are indicated with arrowheads, and HAps with arrow marks. **(B)** FTIR analysis. Indicated peaks: a: OH⁻ ion stretching (3500-3100 cm⁻¹); b: CO_3^{2-} (1350 and 1650 cm⁻¹); c: PO_4^{3-} (1045 and 1087 cm⁻¹, and P—O bending at 550-650 cm⁻¹); d: Fe—O vibration (570 cm⁻¹). **(C)** Magnetization curves.

on the surface of the MNPs (right image). The average size of the HAp nanorods was found to be ~35 nm in length and ~10 nm in width (Fig. 3A).

FTIR analyses of MNPs and HAp-MNPs are shown in Figure 3B. The FTIR spectrum of the MNPs confirms the iron oxide specific peak at 570 cm^{-1} and the broad peak of OH$^-$ ion stretching at 3500-3100 cm^{-1}. The FTIR spectrum of HAp-MNPs show the characteristic bands of PO$_4^{3-}$ groups at 1045 and 1087 cm^{-1}, and the CO$_3^{2-}$ groups at 1350 and 1650 cm^{-1}. In addition, the broad peak observed in the range of 550−650 cm^{-1} shows the P−O bending vibration that overlaps with the Fe−O vibration peak.[44−46]

Hysteresis curves of MNPs and HAp-MNPs are shown in Figure 3C. MNPs exhibit strong saturation magnetisation of 64 emu/g. However, HAp-MNPs have a lower saturation magnetisation of 22 emu/g. As a result of the interaction with hydroxyapatite, the magnetization value of MNPs has decreased by ~65%. This decrease in magnetization was expected due to the non-magnetic hydroxyapatite component surrounding the magnetic iron oxide nanoparticles and blocking the magnetic effect. The synthesis methods and the ratios of the components used during the synthesis define the magnetization value of magnetic HAp nanostructures.[47,48] As a result, the magnetization of HAp-MNPs is sufficient for use in biological applications and higher compared to other studies in the literature in which HAp/MNPs are used as biomaterials.[49]

Characterization of bioinks

FTIR spectra obtained for Gel-MA and Gel-MA/HAp-MNP bioinks are presented in Figure 4A. Gel-MA spectrum
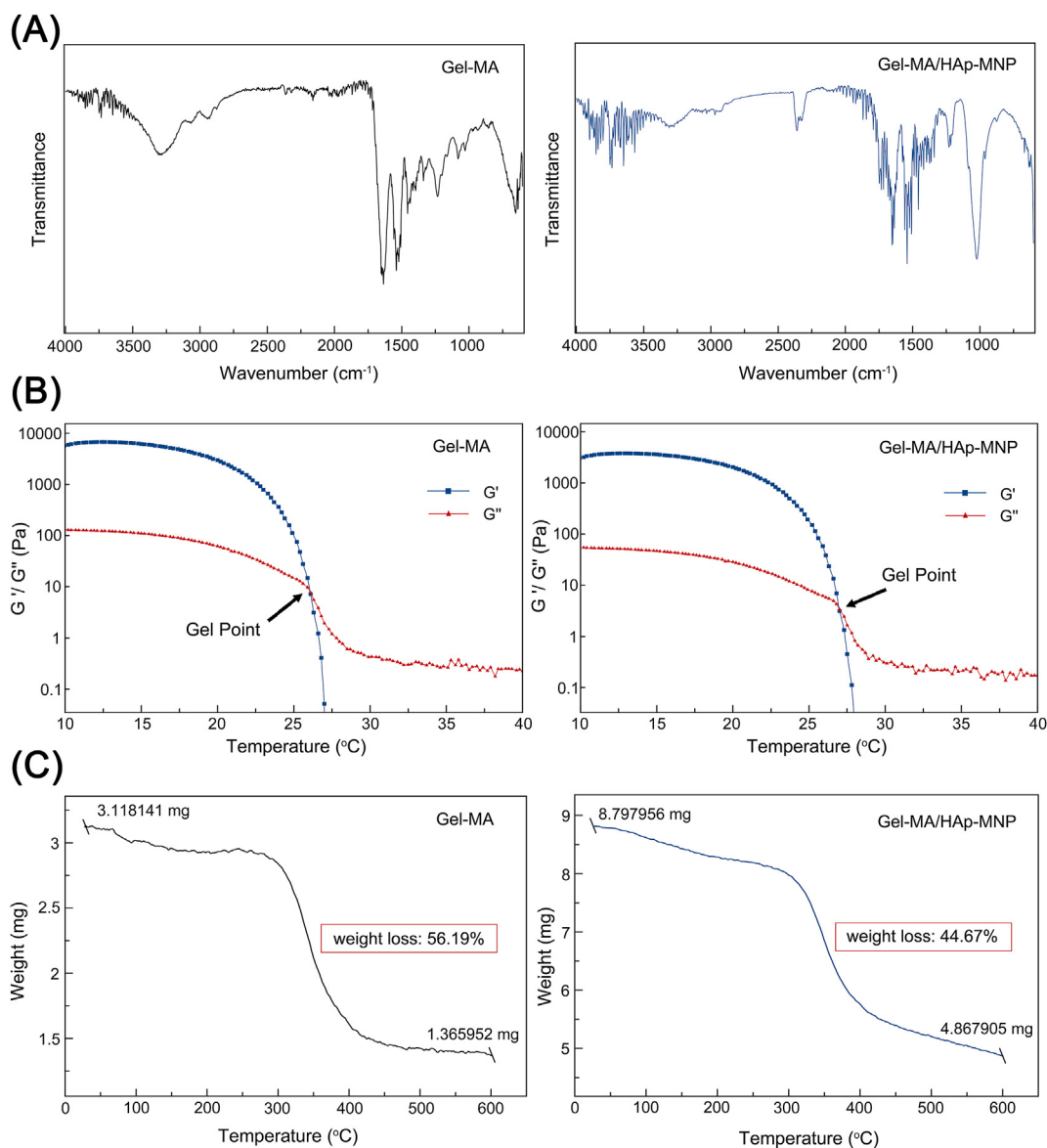
Figure 4 Characterization of Gel-MA and Gel-MA/HAp-MNP bioinks. **(A)** FTIR analysis. **(B)** Effect of temperature on storage modulus (G′) and loss modulus (G″). **(C)** Thermogravimetric analysis.

showed the following specific vibrations: a broad peak with a peak position at 3300 cm^{-1} (common signal for O—H and N—H stretching), 3070 cm^{-1} (N—H), 2940 cm^{-1} (saturated C—H stretch), a strong peak appears at 1650 cm^{-1} (Amide I) and 1550 cm^{-1} (Amide II).[50,51] The FTIR spectra of the Gel-MA/HAp-MNP bioink showed characteristic absorption peaks of the Gel-MA and HAp-MNP functional groups. Peaks at 3300 cm^{-1}, 3070 cm^{-1}, 2940 cm^{-1}, 1650 cm^{-1} and 1550 cm^{-1} are related to Gel-MA. Also the characteristic peaks for PO$_4^{3-}$ at 605 cm^{-1}, 633 cm^{-1}, 970 cm^{-1}, 1030 cm^{-1} and 1090 cm^{-1} are due to the presence of hydroxyapatite component of HAp-MNPs. The sharp peak at 605 cm^{-1} and medium sharp peak at 633 cm^{-1} correspond to the bending vibrations of PO$_4^{3-}$ in HAp and the peaks at 1030 and 1090 cm^{-1} correspond to n3 (asymmetric stretching mode) vibrations of the PO$_4^{3-}$ group.[52,53] Results of the FTIR analysis confirmed the successful chemical modification of gelatin to Gel-MA, and the presence of HAp-MNPs in the composite bioink.

The rheological properties of Gel-MA (12.5%) and Gel-MA/HAp-MNP (12.5%/0.1%) bioinks were measured by cooling the temperature from 40 °C to 10 °C, with 1 °C/min increments. As seen in the Figure 4B, G″ was higher than G′ at 40 °C for both Gel-MA and Gel-MA/HAp-MNP bioinks. By the cooling, G′ and G″ increased and crossed over. This crossover temperature is the gelling point (sol—gel transition temperature) and explains the transition from solution state to the gel state as the temperature decreases. Findings show that the rheological properties of Gel-MA differ with temperature change, as a thermo-sensitive material. While the temperature is just above the gelling points of the bioinks, the storage modulus is at very low values due to the breakdown of the physical networks. While the gelling point of Gel-MA was around 26.5 °C, it was found to be ∼27 °C for Gel-MA/HAp-MNPs (Fig. 4B). This shows that ∼0.5 °C rise in the gelling point of Gel-MA was observed, by the addition of HAp-MNP (0.1%) to the bioink. Rheology results indicate that, above 27 °C both of the bioinks were in liquid form, where the viscosity is too low for accomplishing 3DP. On the other side, below 26 °C both bioinks were in gel form and their viscosity was suitable for performing 3D bioprinting.

The thermal degradation properties of Gel-MA and Gel-MA/HAp-MNP bioinks were evaluated by thermogravimetric analysis, as presented in Figure 4C. Thermograms showed weight loss with rising temperatures and one distinct weight loss stage for both of the bioinks. For Gel-MA, the main stage of weight loss started at ∼320 °C and continued up to 450 °C due to the decomposition of the material,[54] with a calculated weight loss of 56.19% (Fig. 4C). For the Gel-MA/HAp-MNPs, the weight loss started at ∼320 °C and continued up to ∼500 °C, with a lesser amount of weight loss (44.67%), demonstrating significant increase in thermal stability by the incorporation of HAp-MNPs to the Gel-MA bioink. Typically, thermograms of the hydrogels usually show two or three actual losses related to the loss of water molecules, decomposition of the material and burning of organic components.[55,56] On the other hand, the initial stage weight losses of the samples were very low, since they were freeze-dried before the analysis.

## Characterization of 3D-printed constructs

Mechanical and swelling properties, and surface morphologies of the 3D-printed Gel-MA and Gel-MA/HAp-MNP constructs were evaluated. The 3D-printings were performed according to the optimal process parameters given in Table S1. A mechanical compression test was performed to investigate the mechanical properties of 3D printed (cell-devoid) Gel-MA gel, as well as the impact of incorporating HAp-MNPs into Gel-MA constructs. Figure 5A shows the stress—strain curves of 3D printed Gel-MA and Gel-MA/HAp-MNP constructs and their maximum stress (kPa) values. Although both of the groups follow quite a similar path, the maximum values of stress appear to be quite different from each other. Eventually, 3D printed Gel-MA/HAp-MNP construct showed a higher level of compressive strength when compared with that of Gel-MA. The maximum strength value of 3D printed Gel-MA/HAp-MNP (∼20 kPa) was twice as much of the 3D printed Gel-MA construct (9.3 kPa) (Fig. 5A). In other studies, quite analogous changes in mechanical properties are observed by the addition of compositing materials into Gel-MA hydrogels as well.[57,58] Thus, it is anticipated that the chemical interactions between the functional groups of Gel-MA hydrogel and HAp-MNPs could be the cause of improvement in the mechanical compression properties of the gels.

The swelling properties of the hydrogels are mainly dependent on their chemical composition and concentration.[59] The findings from the equilibrium swelling analysis of Gel-MA, Gel-MA/HAp-MNP and Gel-MA + Gel-MA/HAp-MNP specimens crosslinked using three different concentrations of the photoinitiator, Irgacure 2959 (0.1%, 0.25% and 0.5%) are presented in Figure 5B. It is evident from the figure that the swelling ratios of the Gel-MA constructs decreased by the increase in crosslinker concentration from 0.1 to 0.5%, perhaps due to the decrease in mesh size of the GelMA hydrogel network, which may have decreased the diffusion of water into GelMA.[60]

Representative SEM micrographs of the 3D bioprinted and freeze-dried cell-free Gel-MA and Gel-MA/HAp-MNP constructs are demonstrated in Figure 5C and D. The struts (0.5—0.6 mm fiber diameter) of the 3D printed constructs are evident from the images in different magnifications. The 3D printed design model is still preserved, however with some shrinkage and surface deformations due to the freeze-drying step and preparation of specimens prior to SEM analysis. It is also evident that Gel-MA/HAp-MNP constructs have a more textured and dense form, compared with that of Gel-MA constructs (Fig. 5C,D), related to its inorganic content. On the other hand, phase-contrast images (Fig. 6A) confirm that 3D printed constructs preserve their shape without shrinkage or deformation in aqueous conditions.

Characterization of 3D-bioprinted constructs (shape-fidelity and distribution of cells)

The process parameters were optimized carefully for bioprinting the desired cell-laden microtissue constructs. Gel-MA hydrogels of ≥10% concentration permitted bioprinting,[61,62] whereas <10% Gel-MA hydrogels were not
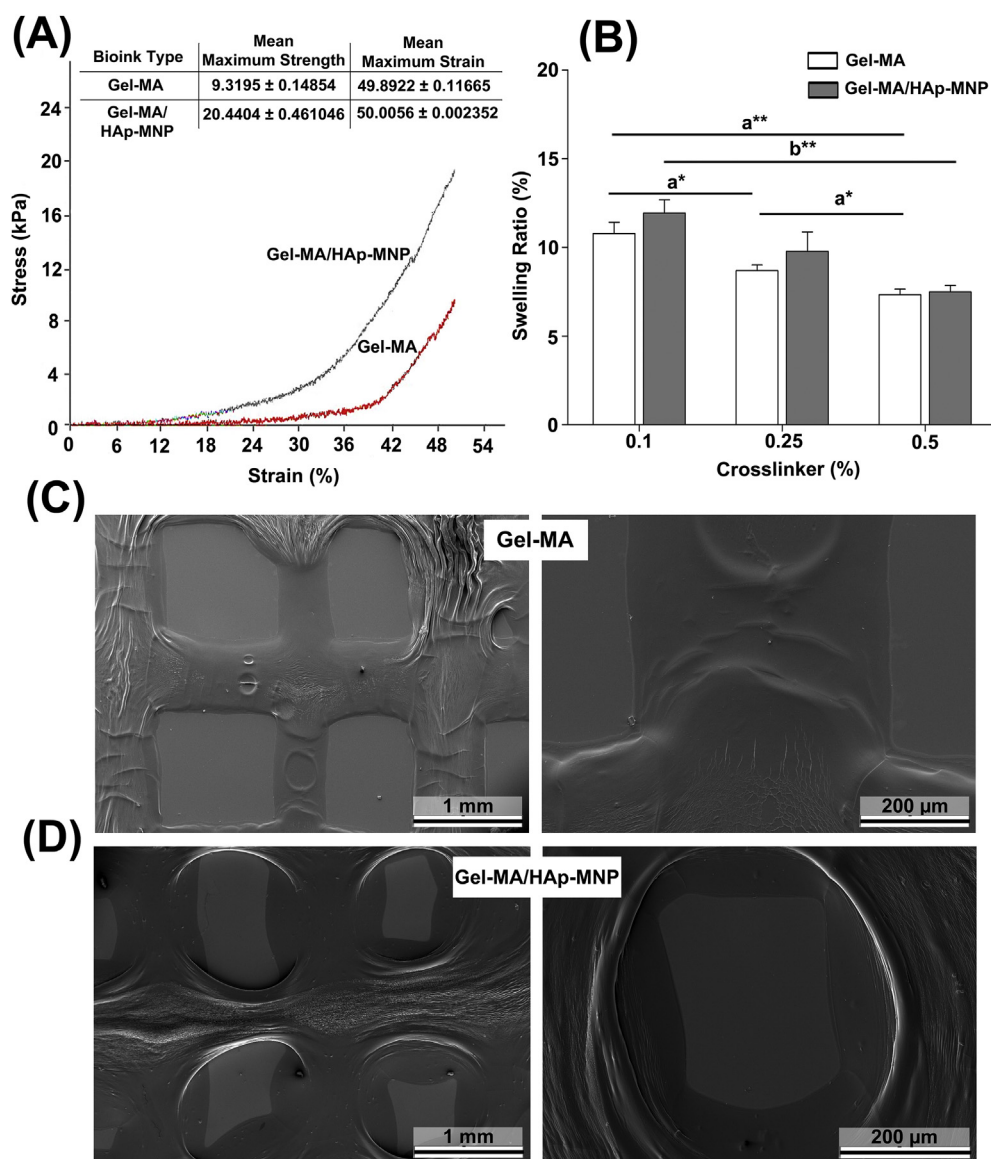
Figure 5 Mechanical and swelling properties of 3D-printed cell-free Gel-MA and Gel-MA/HAp-MNP constructs. **(A)** Compression strength analysis. **(B)** Equilibrium swelling properties of the hydrogels ($n = 3$) ([a,a; b,b; c,c; d,d] $P < 0.05$). **(C, D)** Scanning electron micrographs of 3DP Gel-MA and Gel-MA/HAp-MNP.

suitable for 3D-bioprinting at 25 °C related to their low viscosity. Similar to a previous study,[33] the Gel-MA concentration of 12.5% was found optimal for bioprinting thinner strands with shape fidelity (Fig. 6A,B). It was possible to bioprint mechanically more stable, higher-resolution constructs with hydrogel concentrations >12.5%, however this would require much higher extrusion pressure known to cause cellular damage. Also, high crosslinking of hydrogels could be an obstacle for the migration, proliferation and nutrient transfer of the encapsulated cells.[63] However, precisely homogenous struts of the microtissues possessing viable cells could be fabricated by using the optimized 3D-bioprinting parameters, including the printing speed, extrusion pressure, cartridge temperature, nozzle diameter, radical photoinitiator concentration, and UV exposure time. It was also found that the 3D-bioprinted constructs were mechanically stable

to the applied microfluidic culture conditions for at least two weeks (not shown).

CLM analysis evidently demonstrated that the bioprinted cells (hPDLFs and hOBs) were highly viable and were homogeneously distributed throughout the bioprinted gel construct (Fig. 6C). The distribution and localization of both cell types inside the hybrid periodontal/osteoblastic microtissue were evaluated by using IF microscopy (Fig. 6D). Stromal cell surface marker-1 (STRO-1) is positive for human PDLFs cells found in the periodontal layer,[64] whereas osteocalcin (OSC) is positive for osteoblastic cells located in the osteoblastic layer of the hybrid bilayer construct.[65] It was observed that STRO-1^{+} cells (hPDLFs) and OSC^{+} cells (hOBs) were localized in their own layers at the early stage of culture (Fig. 6D(a)). Subsequently, hOBs and hPDLFs were intertwined in some regions of the construct (Fig. 6D(b),(c)) which could be explained by the
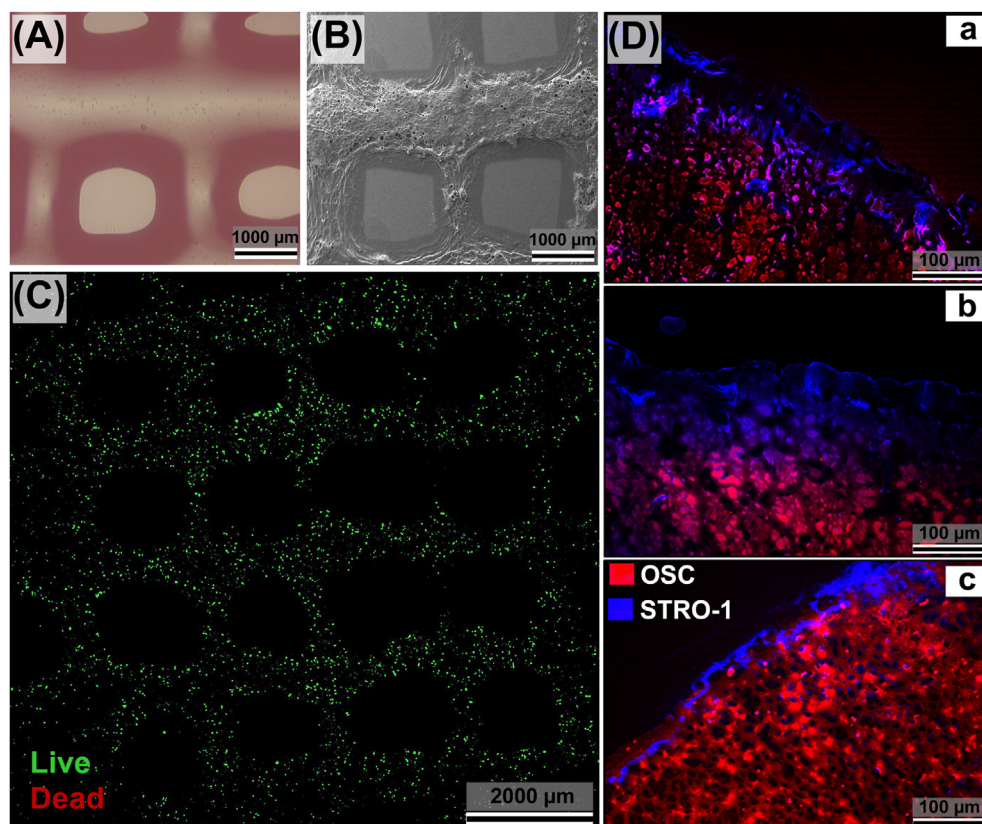
Figure 6 *Morphology of 3D-bioprinted, layered human periodontal/osteoblastic microtissue in microfluidic culture.* **(A)** Phase-contrast, and **(B)** SEM images confirm the shape retention of the constructs. **(C)** CLM shows the homogenous distribution of the viable cells throughout the construct (after 12 h). **(D)** Immunofluorescence micrographs demonstrating the localization of periodontal and osteoblastic layers, and their gradual intervention after 1 day (a), 3 days (b), and 7 days (c) of microfluidic culture (top view). The blue-stained layer (containing STRO-1$^+$ hPDLFs, simulating the periodontal ligament), and the red-stained layer (containing OSC$^+$ hOBs, simulating the alveolar bone) are in close vicinity, and have merged in some locations. Cell densities: hPDLF-laden Gel-MA layer (4.0 $\times$ 10^6 hPDLFs/mL gel); hOB-laden Gel-MA/HAp-MNP layer (4.0 $\times$ 10^6 hOBs/mL gel). Scale bars = 100 μm. Separate images are given in Figure S2.

permeability (consistency) of the bioprinted constructs allowing migration or proliferation of the cells, and/or by the degradation of the gels to some extent under the microfluidic culture conditions. It was observed that mostly the STRO-1$^+$ (blue) hPDLFs migrated to the OSC$^+$ (red) osteoblastic bottom layer (Fig. S2).

## Histologic evaluation of implanted constructs

While the main aim of this study was to develop a multicellular 3D-bioprinted *in vitro* microtissue model of human periodontal ligament-alveolar bone biointerface, the approach incorporates potential *in vivo* implications (*i.e.,* periodontal tissue engineering). For that reason, a preliminary histologic analysis was performed as a first attempt to evaluate the histocompatibility of the 3D-bioprinted acellular constructs. Representative light microscopy images retrieved at 15 and 30 days post-implantations are given in Figure S3. Findings indicated that the constructs subcutaneously implanted into the epigastric groin fascia of Wistar rats demonstrated a moderate level of inflammatory process leading to substantial degradation within the duration of the study without any remarkable sign of fibrous

tissue formations. After 15 days of implantation, the host cell infiltration was evident inside the 3DP-construct accompanied by a gradual degradation from the periphery where capillaries and small blood vessels could be prevalently observed. The remnants of the 3D-bioprinted acellular construct were distinguished after 30 days of implantation; thus this microenvironment could be described as a suitable medium for remodeling (Fig. S3). Prospective studies involving the orthotopic transplantation of 3D-bioprinted cell-laden constructs could perhaps indicate the potential of the designed microtissue for tissue engineering applications.

Tetracycline interactions in microfluidic culture

Alamar blue assay
The results of the Alamar blue assay of 3D-bioprinted hybrid microtissue cultured in the presence or absence of the tetracycline are presented in Figure 7A. Similar to CLM findings (Fig. 6C), Alamar blue results confirmed the cytocompatibility of the bioinks under standard culture not containing tetracycline. Secondly, results indicated that tetracycline concentrations used in the study did not show
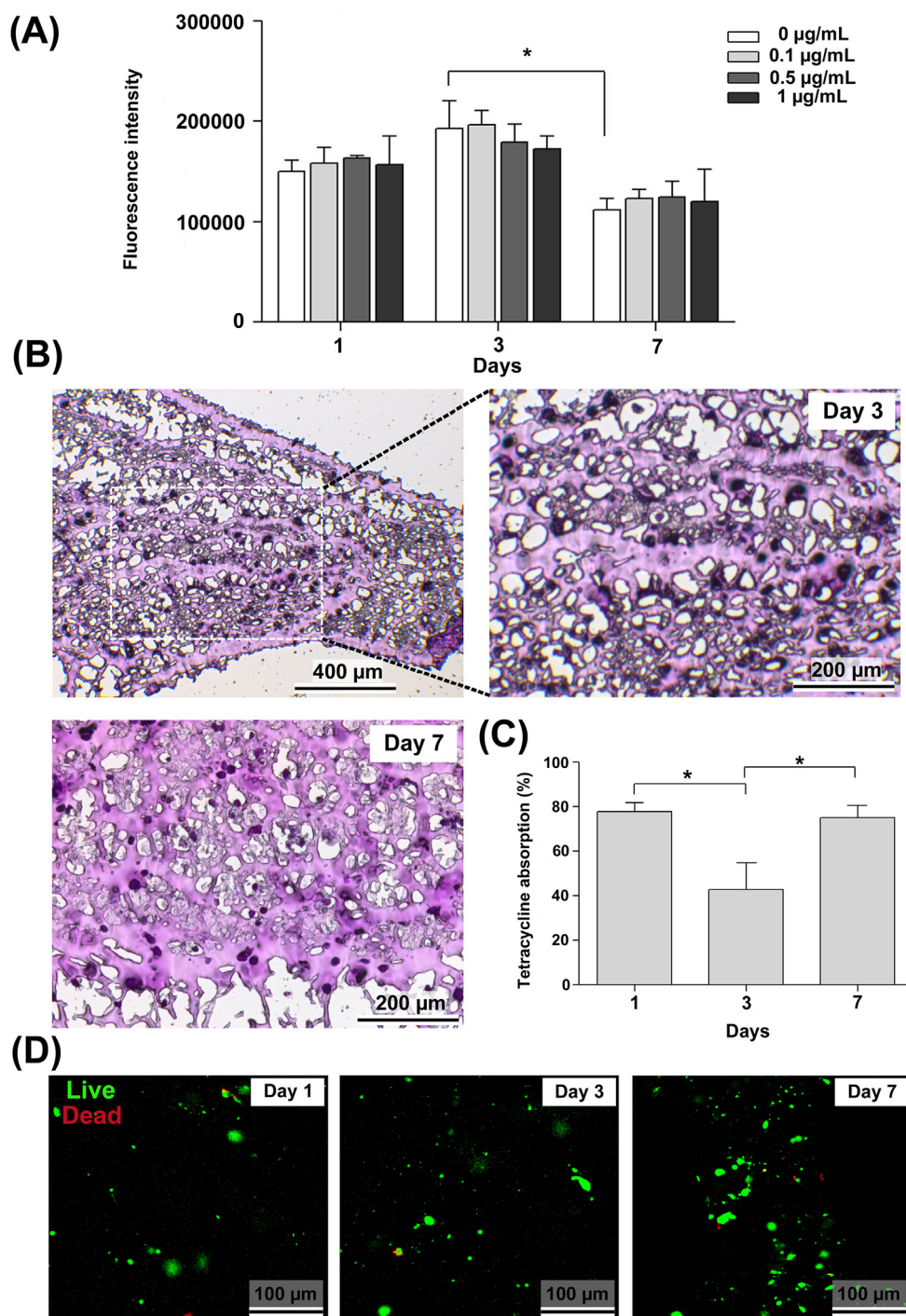
Figure 7 Human periodontal/osteoblastic microtissue exposed to tetracycline in microfluidic culture. **(A)** Cell viability of the constructs exposed to different doses of tetracycline (0–1.0 μg/mL) was measured by Alamar blue assay, and the groups were compared with time change using the two-way ANOVA and Bonferroni post-hoc test (*$P < 0.05$) for $n \geq 3$ individual repeats. **(B)** Representative histology images of the layered microtissues exposed to 1.0 μg/mL tetracycline in microfluidic culture for 3 and 7 days. Micrographs demonstrate homogeneous distribution of cells encapsulated inside the bioprinted constructs. PAS-stained (magenta-coloured) denser matrix with lesser empty spaces in the sections at day 7 (compared with day 3) resembles the production of glycosaminoglycans. **(C)** Tetracycline absorption levels of the perio/osteo microtissues inside microfluidic chip. The data was normalized to cell-devoid 3D-printed gels. Groups were compared using the one-way ANOVA and Bonferroni post-hoc tests (*$P < 0.05$). **(D)** CLM images of the periodontal/osteoblastic microtissues retrieved after 1, 3 and 7 days of microfluidic culture containing tetracycline, indicating the viability of cells at all time-points. Green staining apparently shows the uptake of the calcein reagent by the living cells. Dead cells stained in red color (ethidium homodimer labelling) are rarely observed even after 7 days.

remarkable toxic effect on the periodontal/osteoblastic microtissue. In general, there was no significant difference between the fluorescence intensity of the groups at time points. The fluorescence intensity for each group at day 3 was found to be the highest, whereas a dose-dependent, but insignificant decrease in cell viability was also observed at day 3. This perhaps could be explained by the proliferation of cells between day 1 and 3 inside the bioprinted constructs to a certain extent. On the other side, the observed decrease in fluorescence intensity from day 3 to day 7 ($P > 0.05$) could be due to the formed hypoxic conditions caused by the proliferated cells.[66,67] Therefore, it is possible to suggest for further studies that the optimal culture time frame could be roughly around three days with the developed multi-cellular microtissue.

Histochemistry analysis

Periodic acid—Schiff (PAS) staining was performed to evaluate the density and distribution of cells, as well as the polysaccharides in the hydrogel microtissue. As known, PAS stains carbohydrate-rich macromolecules, including chondroitin sulfate which is a prevalent glycosaminoglycan contributing to the adhesion of periodontal ligament to the alveolar bone.[68] Figure 7B shows histology images of the two-layered microtissues exposed to 1.0 μg/mL tetracycline in microfluidic culture for 3 and 7 days. A homogenous distribution of cells encapsulated within the 3D-bioprinted Gel-MA-based constructs can be observed from the micrographs. Secondly, compared with day 3, the PAS-stained (magenta-coloured) denser matrix with lesser empty spaces at day 7 may suggest the preliminary production of glycosaminoglycans (Fig. 7B).

As known, collagen fibers of the PDL undergo partial intrafibrillar mineralization inside the alveolar bone forming a continuous non-mineralized/mineralized structure (the Sharpey's fibers) (Fig. S1).[1,2] Histological evaluations did not demonstrate collagenous fiber insertions between the two bioprinted tissue layers. As a matter of fact, we did not expect such formations within such a relatively short period of culture time.

Tetracycline absorption

Drug absorption is among the analysis performed on microfluidic tissue systems.[69–71] The percentage of drug absorption was calculated using the cell culture supernatant retrieved from the waste medium at predetermined time intervals. The results given in Figure 7C indicated that tetracycline absorption was ∼78% and ∼75% at day 1 and 7, respectively. Even though these preliminary results are consistent with the *in vivo* tetracycline absorption data,[72] further studies are needed to confirm such results. The tetracycline absorption on day 3 (∼43%) was found to be lower than that of day 1 and 7 ($P < 0.05$), which may be explained by several events. Tetracycline-metal complexation,[73] such as chelation with Ca^{2+} and Fe^{3+} cations (contained respectively in HAp and MNPs in the cell encapsulation matrix) may not be a strong possibility, since the data was normalized to cell-devoid 3D-printed gels. Binding of tetracycline to proteins or nucleic acids accumulated as cellular waste metabolites could have impaired drug absorption for a certain period of culture time,[74]

which in due course have disappeared (by discharge) through swelling of the composite bioprinting matrix.

In principle, the efficacy of a drug candidate developed for the treatment of any infection can be evaluated using a 3D microtissue infection model. For example, Ortega-Prieto et al[75] have developed a 3D-microfluidic liver culture system infected with Hepatitis B virus (HBV) to evaluate curative therapies for HBV infection. Molecular and metabolic changes in 3D-microfluidic liver cultures were investigated. In another study, the airway microfluidic culture system as influenza A infection model was created by Si et al.[76] Analyses of various cytokines and chemokines associated with influenza in the presence of nafamostat drug were performed. To our knowledge, a 3DBP multi-cellular microtissue model resembling human periodontal ligament-alveolar bone biointerface has not been developed to date. The presented microtissue model can be advanced as an infection model, which may provide a platform for the evaluation of interactive effects of drugs on cells in the context of a bioartificial periodontal/osteoblastic tissue microenvironment in the future.

CLM analysis

The viability and distribution of the cells in the three-dimensional bioprinted structure cultured in the presence of tetracycline were visualized using CLM at the predetermined time intervals. Confocal microscopy images of the periodontal/osteoblastic microtissue at day 1, day 3 and day 7 are presented in Figure 7D. Live cells stain green while dead cells stain red color. The results show that the cells at all time points were homogeneously distributed in the bioprinted gel structure. In addition, it is clearly seen that green staining showing calcein reagent taken by living cells was highly intense at all time points. On the other hand, the small amount of red-stained cells that indicate the ethidium homodimer labeling of the dead cells were observed on day 3 and 7 (Fig. 7D). These results were found to be compatible with the Alamar blue cell viability data (Fig. 7A). The results indicated that a viable human periodontal/osteoblastic microtissue could be fabricated by using 3D-bioprinting which was exposed to relatively high flow-rate culture conditions.

Conclusions

In conclusion, we have attempted to develop a 3D-bioprinted microtissue model of periodontal ligament-alveolar bone biointerface for the first time. The periodontal ligament layer was generated by bioprinting hPDLFs laden Gel-MA bioink, whereas the alveolar bone layer was formed by bioprinting hOBs laden Gel-MA/HAp-MNP composite bioink. The double-layered microtissue construct was cultured under flow in a microfluidic platform for over ten days without significant loss of shape fidelity. IF analysis showed the cohesion of STRO-1^+ hPDLFs containing PDL layer with the OSC$^+$ hOBs containing mineralized layer in time, demonstrating some permeability of the printed constructs to cell migration. Preliminary evaluation of model drug interactions indicated that tetracycline concentrations used in the study did not show remarkable toxic effect

on the microtissue construct. Prospective culture studies to be performed under the magnetic field could reveal to what extent magnetically sensitive Gel-MA/HAp-MNP composite tissue layer will direct cell behavior (i.e., orthodontic movements experienced by the PDL). By assembling other components of the microenvironment (e.g., other cell types, vascularization, innervation and immune system) onto the developed PDL-AB bio-interface could possibly lead to a preclinical platform for the evaluation of interactive effects of drugs on cells in the context of an emulated bioartificial periodontal/ osteoblastic tissue microenvironment.

Author contributions

Murat Taner Vurat: concept and design, experimental studies, data acquisition, data analysis, statistical analysis, manuscript preparation. **Şükran Şeker:** concept and design, experimental studies, data acquisition, data analysis, statistical analysis, manuscript preparation. **Özge Lalegül-Ülker:** concept and design, experimental studies, data acquisition, data analysis, manuscript preparation. **Mahmut Parmaksiz:** concept and design, literature search, data acquisition, data analysis. **Ayşe Eser Elçin:** concept and design, experimental studies, data acquisition, data analysis, statistical analysis, manuscript preparation. **Yaşar Murat Elçin:** supervision, resources, concept and design, literature search, manuscript preparation, manuscript editing and manuscript review.

Conflict of interests

Funding

Appendix A. Supplementary data

Supplementary data to this article can be found online at https://doi.org/10.1016/j.gendis.2020.11.011.

References

1. Jiang N, Guo W, Chen M, et al. Periodontal ligament and alveolar bone in health and adaptation: tooth movement. *Front Oral Biol*. 2016;18:1—8.
2. de Jong T, Bakker AD, Everts V, Smit TH. The intricate anatomy of the periodontal ligament and its development: lessons for periodontal regeneration. *J Periodontal Res*. 2017;52(6):965—974.
3. Pihlstrom BL, Michalowicz BS, Johnson NW. Periodontal diseases. *Lancet*. 2005;366(9499):1809—1820.
4. World Health Organization. *Newsroom/Fact sheets/Detail/Oral health*. WHO; 2020. Accessed May 5, 2020.
5. Weinreb M, Nemcovsky CE. In vitro models for evaluation of periodontal wound healing/regeneration. *Periodontol 2000*. 2015;68(1):41—54.
6. Inanc B, Elcin AE, Elcin YM. Osteogenic induction of human periodontal ligament fibroblasts under two- and three-dimensional culture conditions. *Tissue Eng*. 2006;12(2):257—266.
7. Inanç B, Elçin AE, Koç A, Baloş K, Parlar A, Elçin YM. Encapsulation and osteoinduction of human periodontal ligament fibroblasts in chitosan-hydroxyapatite microspheres. *J Biomed Mater Res A*. 2007;82(4):917—926.
8. Inanç B, Arslan YE, Seker S, Elçin AE, Elçin YM. Periodontal ligament cellular structures engineered with electrospun poly(DL-lactide-co-glycolide) nanofibrous membrane scaffolds. *J Biomed Mater Res A*. 2009;90(1):186—195.
9. Berahim Z, Moharamzadeh K, Jowett AK, Rawlinson A. Evaluation of osteogenic and cementogenic potential of periodontal ligament fibroblast spheroids using a three-dimensional in vitro model of periodontium. *Int J Dent*. 2015; 2015:605813.
10. Pellegrini G, Seol YJ, Gruber R, Giannobile WV. Pre-clinical models for oral and periodontal reconstructive therapies. *J Dent Res*. 2009;88(12):1065—1076.
11. Marchesan J, Girnary MS, Jing L, et al. An experimental murine model to study periodontitis. *Nat Protoc*. 2018; 13(10):2247—2267.
12. Wikswo JP, Block FE 3rd, Cliffel DE, et al. Engineering challenges for instrumenting and controlling integrated organ-on-chip systems. *IEEE Trans Biomed Eng*. 2013;60(3):682—690.
13. Bhatia SN, Ingber DE. Microfluidic organs-on-chips. *Nat Biotechnol*. 2014;32(8):760—772.
14. Shih HP, Zhang X, Aronov AM. Drug discovery effectiveness from the standpoint of therapeutic mechanisms and indications. *Nat Rev Drug Discov*. 2018;17(1):19—33.
15. Watson DE, Hunziker R, Wikswo JP. Fitting tissue chips and microphysiological systems into the grand scheme of medicine, biology, pharmacology, and toxicology. *Exp Biol Med (Maywood)*. 2017;242(16):1559—1572.
16. Ghaemmaghami AM, Hancock MJ, Harrington H, Kaji H, Khademhosseini A. Biomimetic tissues on a chip for drug discovery. *Drug Discov Today*. 2012;17(3-4):173—181.
17. Elçin YM. Special issue: organs-on-chips & 3D-bioprinting technologies for personalized medicine. *Stem Cell Rev Rep*. 2017;13(3):319—320.
18. Ronaldson-Bouchard K, Vunjak-Novakovic G. Organs-on-a-chip: a fast track for engineered human tissues in drug development. *Cell Stem Cell*. 2018;22(3):310—324.
19. Conant G, Lai BFL, Lu RXZ, Korolj A, Wang EY, Radisic M. High-content assessment of cardiac function using heart-on-a-chip devices as drug screening model. *Stem Cell Rev Rep*. 2017; 13(3):335—346.
20. van den Broek LJ, Bergers LIJC, Reijnders CMA, Gibbs S. Progress and future prospectives in skin-on-chip development with emphasis on the use of different cell types and technical challenges. *Stem Cell Rev Rep*. 2017;13(3): 418—429.
21. Bein A, Shin W, Jalili-Firoozinezhad S, et al. Microfluidic organ-on-a-chip models of human intestine. *Cell Mol Gastroenterol Hepatol*. 2018;5(4):659—668.
22. Young AK, Moyle-Heyrman G, Kim JJ, Burdette JE. Microphysiologic systems in female reproductive biology. *Exp Biol Med (Maywood)*. 2017;242(17):1690—1700.
23. Neal EH, Marinelli NA, Shi Y, et al. A simplified, fully defined differentiation scheme for producing blood-brain barrier endothelial cells from human iPSCs. *Stem Cell Reports*. 2019;12(6): 1380—1388.

24. Sontheimer-Phelps A, Hassell BA, Ingber DE. Modelling cancer in microfluidic human organs-on-chips. *Nat Rev Cancer*. 2019; 19(2):65–81.

25. Murphy SV, Atala A. 3D bioprinting of tissues and organs. *Nat Biotechnol*. 2014;32(8):773–785.

26. Jungst T, Smolan W, Schacht K, Scheibel T, Groll J. Strategies and molecular design criteria for 3D printable hydrogels. *Chem Rev*. 2016;116(3):1496–1539.

27. Cidonio G, Glinka M, Dawson JI, Oreffo ROC. The cell in the ink: improving biofabrication by printing stem cells for skeletal regenerative medicine. *Biomaterials*. 2019;209:10–24.

28. Miri AK, Mostafavi E, Khorsandi D, Hu SK, Malpica M, Khademhosseini A. Bioprinters for organs-on-chips. *Biofabrication*. 2019;11(4):042002.

29. Vurat MT, Ergun C, Elçin AE, Elçin YM. 3D-Bioprinting of tissue models with customized bioinks. *Adv Exp Med Biol*. 2020;1249: 67–84.

30. Yi HG, Lee H, Cho DW. 3D Printing of organs-on-chips. *Bioengineering (Basel)*. 2017;4(1):10.

31. Gold K, Gaharwar AK, Jain A. Emerging trends in multiscale modeling of vascular pathophysiology: organ-on-a-chip and 3D printing. *Biomaterials*. 2019;196:2–17.

32. Mastikhina O, Moon BU, Williams K, et al. Human cardiac fibrosis-on-a-chip model recapitulates disease hallmarks and can serve as a platform for drug testing. *Biomaterials*. 2020; 233:119741.

33. Raveendran NT, Vaquette C, Meinert C, Ipe DS, Ivanovski S. Optimization of 3D bioprinting of periodontal ligament cells. *Dent Mater*. 2019;35(12):1683–1694.

34. Santos RS, Macedo RF, Souza EA, Soares RS, Feitosa DS, Sarmento CF. The use of systemic antibiotics in the treatment of refractory periodontitis: a systematic review. *J Am Dent Assoc*. 2016;147(7):577–585.

35. Golub LM, Lee HM. Periodontal therapeutics: current host-modulation agents and future directions. *Periodontol 2000*. 2020;82(1):186–204.

36. Hai NH, Phu ND, Luong NH, et al. Mechanism for sustainable magnetic nanoparticles under ambient conditions. *J Kor Phys Soc*. 2008;52(5):1327–1331.

37. Lalegül-Ülker Ö, Vurat MT, Elçin AE, Elçin YM. Magnetic silk fibroin composite nanofibers for biomedical applications: fabrication and evaluation of the chemical, thermal, mechanical, and in vitro biological properties. *J Appl Polym*. 2019;136:48040.

38. Sneha M, Sundaram NM, Kandaswamy A. Synthesis and characterization of magnetite/hydroxyapatite tubes using natural template for biomedical applications. *Bull Mater Sci*. 2016;39(2): 509–517.

39. Van Den Bulcke AI, Bogdanov B, De Rooze N, Schacht EH, Cornelissen M, Berghmans H. Structural and rheological properties of methacrylamide modified gelatin hydrogels. *Biomacromolecules*. 2000;1(1):31–38.

40. Inanç B, Elçin AE, Unsal E, Balos K, Parlar A, Elçin YM. Differentiation of human embryonic stem cells on periodontal ligament fibroblasts in vitro. *Artif Organs*. 2008;32(2): 100–109.

41. Seker S, Elçin AE, Yumak T, Sınağ A, Elçin YM. In vitro cytotoxicity of hydrothermally synthesized ZnO nanoparticles on human periodontal ligament fibroblast and mouse dermal fibroblast cells. *Toxicol In Vitro*. 2014;28(8):1349–1358.

42. Sakellari D, Goodson JM, Kolokotronis A, Konstantinidis A. Concentration of 3 tetracyclines in plasma, gingival crevice fluid and saliva. *J Clin Periodontol*. 2000;27(1):53–60.

43. Koç A, Elçin AE, Elçin YM. Ectopic osteogenic tissue formation by MC3T3-E1 cell-laden chitosan/hydroxyapatite composite scaffold. *Artif Cell Nanomed Biotechnol*. 2016;44(6): 1440–1447.

44. Chandrasekar A, Sagadevan S, Dakshnamoorthy A. Synthesis and characterization of nano-hydroxyapatite (n-HAP) using the wet chemical technique. *Int J Phys Sci*. 2013;8(30):1639–1645.

45. Mujahid M, Sarfraz S, Amin S. On the formation of hydroxyapatite nano crystals prepared using cationic surfactant. *Mater Res*. 2015;18:468–472.

46. Yusoff HM, Salimi MN, Jamlos MF. Synthesis of superparamagnetic hydroxyapatite core-shell nanostructure by a rapid sol-gel route. *e-J Surf Sci Nanotech*. 2017;15:121–126.

47. Wu HC, Wang TW, Sun JS, Wang WH, Lin FH. A novel biomagnetic nanoparticle based on hydroxyapatite. *Nanotechnology*. 2007;18(16):165601.

48. Mondal S, Manivasagan P, Bharathiraja S, et al. Magnetic hydroxyapatite: a promising multifunctional platform for nanomedicine application. *Int J Nanomedicine*. 2017;12: 8389–8410.

49. Sneha M, Sundaram NM. Preparation and characterization of an iron oxide-hydroxyapatite nanocomposite for potential bone cancer therapy. *Int J Nanomedicine*. 2015;10(Suppl 1): 99–106.

50. Rahali K, Ben Messaoud G, Kahn CJF, et al. Synthesis and characterization of nanofunctionalized gelatin methacrylate hydrogels. *Int J Mol Sci*. 2017;18(12):2675.

51. Modaresifar K, Hadjizadeh A, Niknejad H. Design and fabrication of GelMA/chitosan nanoparticles composite hydrogel for angiogenic growth factor delivery. *Artif Cells Nanomed Biotechnol*. 2018;46(8):1799–1808.

52. Mondal S, Manivasagan P, Bharathiraja S, et al. Hydroxyapatite coated iron oxide nanoparticles: a promising nanomaterial for magnetic hyperthermia cancer treatment. *Nanomaterials (Basel)*. 2017;7(12):426.

53. Vurat MT, Elçin AE, Elçin YM. Osteogenic composite nanocoating based on nanohydroxyapatite, strontium ranelate and polycaprolactone for titanium implants. *Trans Nonferrous Met Soc China*. 2018;28:1763–1773.

54. Zhou L, Tan G, Tan Y, Wang H, Liao J, Ning C. Biomimetic mineralization of anionic gelatin hydrogels: effect of degree of methacrylation. *RSC Adv*. 2014;4(42):21997–22008.

55. Aldana AA, Malatto L, Rehman MAU, Boccaccini AR, Abraham GA. Fabrication of gelatin methacrylate (GelMA) scaffolds with nano-and micro-topographical and morphological features. *Nanomaterials (Basel)*. 2019;9(1):120.

56. Sadeghi M, Heidari B. Crosslinked graft copolymer of methacrylic acid and gelatin as a novel hydrogel with pH-responsiveness properties. *Materials (Basel)*. 2011;4(3):543–552.

57. Ho SP, Kurylo MP, Fong TK, et al. The biomechanical characteristics of the bone-periodontal ligament-cementum complex. *Biomaterials*. 2010;31(25):6635–6646.

58. Zuo Y, Liu X, Wei D, et al. Photo-cross-linkable methacrylated gelatin and hydroxyapatite hybrid hydrogel for modularly engineering biomimetic osteon. *ACS Appl Mater Interfaces*. 2015; 7(19):10386–10394.

59. Serafim A, Tucureanu C, Petre DG, et al. One-pot synthesis of superabsorbent hybrid hydrogels based on methacrylamide gelatin and polyacrylamide. Effortless control of hydrogel properties through composition design. *New J Chem*. 2014;38: 3112–3126.

60. Bukhari SMH, Khan S, Rehanullah M, Ranjha NM. Synthesis and characterization of chemically cross-linked acrylic acid/gelatin hydrogels: effect of pH and composition on swelling and drug release. *Int J Polym Sci*. 2015:1–15.

61. Yin J, Yan M, Wang Y, Fu J, Suo H. 3D bioprinting of low-concentration cell-laden gelatin methacrylate (GelMA) bioinks with a two-step cross-linking strategy. *ACS Appl Mater Interfaces*. 2018;10(8):6849–6857.

62. Schuurman W, Levett PA, Pot MW, et al. Gelatin-methacrylamide hydrogels as potential biomaterials for fabrication

of tissue-engineered cartilage constructs. *Macromol Biosci*. 2013;13(5):551—561.

63. Levato R, Visser J, Planell JA, Engel E, Malda J, Mateos-Timoneda MA. Biofabrication of tissue constructs by 3D bioprinting of cell-laden microcarriers. *Biofabrication*. 2014; 6(3):035020.

64. Park JC, Kim JM, Jung IH, et al. Isolation and characterization of human periodontal ligament (PDL) stem cells (PDLSCs) from the inflamed PDL tissue: in vitro and in vivo evaluations. *J Clin Periodontol*. 2011;38(8):721—731.

65. Arpornmaeklong P, Brown SE, Wang Z, Krebsbach PH. Phenotypic characterization, osteoblastic differentiation, and bone regeneration capacity of human embryonic stem cell—derived mesenchymal stem cells. *Stem Cell Dev*. 2009; 18(7):955—968.

66. Divieto C, Sassi MP. A first approach to evaluate the cell dose in highly porous scaffolds by using a nondestructive metabolic method. *Future Sci OA*. 2015;1:58.

67. Zhou H, Weir MD, Xu HHK. Effect of cell seeding density on proliferation and osteodifferentiation of umbilical cord stem cells on calcium phosphate cement-fiber scaffold. *Tissue Eng Part A*. 2011;17(21-22):2603—2613.

68. Fujii T, Hirabayashi Y. Histochemical studies of glycosaminoglycans in developing periodontal ligaments of ICR mice. *Anat Rec*. 1999;254(4):465—473.

69. Dai J, Hamon M, Jambovane S. Microfluidics for antibiotic susceptibility and toxicity testing. *Bioengineering (Basel)*. 2016;3(4):25.

70. Jie M, Li HF, Lin L, Zhang J, Lin JM. Integrated microfluidic system for cell co-culture and simulation of drug metabolism. *RSC Adv*. 2016;6:54564—54572.

71. An F, Qu Y, Luo Y, et al. A laminated microfluidic device for comprehensive preclinical testing in the drug ADME process. *Sci Rep*. 2016;6:25022.

72. Agwuh KN, MacGowan A. Pharmacokinetics and pharmacodynamics of the tetracyclines including glycylcyclines. *J Antimicrob Chemother*. 2006;58(2):256—265.

73. Pulicharla R, Hegde K, Brar SK, Surampalli RY. Tetracyclines metal complexation: significance and fate of mutual existence in the environment. *Environ Pollut*. 2017;221:1—14.

74. Neuvonen PJ. Interactions with the absorption of tetracyclines. *Drugs*. 1976;11(1):45—54.

75. Ortega-Prieto AM, Skelton JK, Wai SN, et al. 3D microfluidic liver cultures as a physiological preclinical tool for hepatitis B virus infection. *Nat Commun*. 2018;9(1):682.

76. Si L, Prantil-Baun R, Benam KH, et al. Discovery of influenza drug resistance mutations and host therapeutic targets using a human airway chip. *BioRxiv*. 2019:685552.